AGU PUBLICATIONS

Geochemistry, Geophysics, Geosystems

RESEARCH ARTICLE
10.1002/2016GC006633

Bubble formation and decrepitation control the CO_2 content of olivine-hosted melt inclusions

J. Maclennan[1,2]

[1]Department of Earth Sciences, University of Cambridge, UK, [2]Woods Hole Oceanographic Institution, Woods Hole, USA

Key Points:
- The CO_2 contents of olivine-hosted melt inclusions do not, in general, record their entrapment pressures
- Post-entrapment bubble growth and decrepitation control the distribution of CO_2 in the inclusion system
- Model results indicate that, in rare cases, bubble-bearing melt inclusions may be able to record entrapment pressures of up to 500 MPa

Supporting Information:
- Supporting Information S1
- Data Set S1
- Movie S1
- Movie S2
- Movie S3

Correspondence to:
J. Maclennan,
jcm1004@cam.ac.uk

Citation:
Maclennan, J. (2017), Bubble formation and decrepitation control the CO_2 content of olivine-hosted melt inclusions, *Geochem. Geophys. Geosyst.*, *18*, 597–616, doi:10.1002/2016GC006633.

Received 6 SEP 2016
Accepted 16 JAN 2017
Accepted article online 25 JAN 2017
Published online 16 FEB 2017

Abstract The CO_2 contents of olivine-hosted melt inclusions have previously been used to constrain the depth of magma chambers in basaltic systems. However, the vast majority of inclusions have CO_2 contents which imply entrapment pressures that are significantly lower than those obtained from independent petrological barometers. Furthermore, a global database of melt inclusion compositions from low H_2O settings, indicates that the distribution of saturation pressures varies surprisingly little between mid-ocean ridges, ocean islands, and continental rift zones. 95% of the inclusions in the database have saturation pressures of 200 MPa or less, indicating that melt inclusion CO_2 does not generally provide an accurate estimate of magma chamber depths. A model of the *P-V-T-X* evolution of olivine-hosted melt inclusions was developed so that the properties of the inclusion system could be tracked as the hosts follow a model *P-T* path. The models indicate that the principal control on the saturation of CO_2 in the inclusion and the formation of vapor bubbles is the effect of postentrapment crystallization on the major element composition of the inclusions and how this translates into variation in CO_2 solubility. The pressure difference between external melt and the inclusion is likely to be sufficiently high to cause decrepitation of inclusions in most settings. Decrepitation can account for the apparent mismatch between CO_2-based barometry and other petrological barometers, and can also account for the observed global distribution of saturation pressures. Only when substantial postentrapment crystallization occurs can reconstructed inclusion compositions provide an accurate estimate of magma chamber depth.

1. Introduction

The solubility of CO_2 in basaltic melts is a strong function of pressure [*Mysen et al*., 1975; *Stolper and Holloway*, 1988]. It has long been realized that the CO_2 content of olivine-hosted melt inclusion may, therefore, preserve information about the pressure of inclusion entrapment [*Anderson and Brown*, 1993]. These pressures may then be related to the depth of olivine growth in magma bodies, and compared with independent petrological and geophysical constraints on the positions of magma chambers under active volcanic systems [*Anderson and Brown*, 1993; *Metrich and Wallace*, 2008; *Shaw et al*., 2010; *Wanless and Shaw*, 2012]. It is commonly understood that the melt inclusion CO_2 can only provide a minimum estimate of the depth of entrapment because melts may have been CO_2 undersaturated when the host olivines grew [*Metrich and Wallace*, 2008]. Rare suites of apparently CO_2 undersaturated inclusions provide important constraints on the CO_2 contents of mantle melts and their source regions [*Saal et al*., 2002]. Given these constraints on the distribution of CO_2 contents of mantle melts and geophysical constraints on the depth range of storage zones in magmatic systems, it is likely that inclusions are commonly trapped from CO_2-saturated melt [*Metrich and Wallace*, 2008]. This finding has encouraged the use of olivine-hosted melt inclusions as barometers in basaltic systems [*Shaw et al*., 2010; *Wanless and Shaw*, 2012].

The composition of olivine-hosted melt inclusions is modified by processes that occur after their entrapment. Postentrapment crystallization of olivine on the inclusion walls changes the major element composition of the remaining liquid and raises the concentrations of all elements that are incompatible in olivine. The concentrations of certain elements can also be influenced by diffusive exchange. Fe-Mg interdiffusion can cause significant Fe loss from inclusions after postentrapment crystallization [*Gaetani and Watson*, 2000; *Danyushevsky*, 2002]. Rapid diffusion of H species through olivine allows for rapid re-equilibration of the inclusion with the external melt, leading to both dehydration [*Massare et al*., 2002; *Chen et al*., 2011; *Gaetani et al*., 2012] and hydration [*Hartley et al*., 2015] of inclusions.

Many melt inclusions are also observed to contain vapor bubbles and it is likely that most of these bubbles form after entrapment of the inclusion. Bubbles may also be incorporated into the inclusion at the time of entrapment, but such heterogeneous entrapment appears to be relatively rare in natural sample sets [*Hartley et al*., 2014]. The bubbles observed in melt inclusions are sometimes referred to as shrinkage bubbles because differential thermal contraction of host olivine and melt can lower pressure in the inclusion and generate CO_2 saturation [*Tait*, 1992; *Lowenstern*, 1995]. Postentrapment crystallization may also play a role in formation of these bubbles [*Roedder*, 1984]. Crystallization of olivine on the inclusion walls simultaneously lowers the pressure and raises the CO_2 content in the liquid of the inclusion, favoring saturation [*Steele-Macinnis et al*., 2011; *Sides et al*., 2014; *Aster et al*., 2016]. Another important feature of postentrapment crystallization is that it modifies the major element composition of the melt. The solubility of CO_2 in basalts is controlled not only by pressure, but also by major element composition [*Dixon et al*., 1995; *Shishkina et al*., 2014]. The models presented later in this paper indicate that this effect is perhaps the dominant cause of bubble formation in olivine-hosted melt inclusions.

When a vapor bubble forms in an olivine-hosted melt inclusion it can sequester a large proportion of the CO_2 that was initially dissolved in the melt at the time of entrapment [*Anderson and Brown*, 1993]. A number of approaches have been used to reconstruct the original composition of the inclusion at the time of entrapment by adding the mass of CO_2 contained in the bubble back into the inclusion glass. Some studies have based this reconstruction upon measurements of the relative volumes of bubbles and inclusions and assumption of equilibration between the analyzed glass CO_2 content and the bubble at some fixed *P-T* conditions [*Anderson and Brown*, 1993; *Shaw et al*., 2010]. More recently the mass of CO_2 present in the bubbles has been estimated using either cooling stages or Raman spectroscopy [*Esposito et al*., 2011; *Hartley et al*., 2014; *Moore et al*., 2015; *Wallace et al*., 2015]. These additional measurements help to better constrain the CO_2 budget of the inclusion system. Another approach involved experimental heating of olivine-hosted inclusions, with the aim of rehomogenizing the inclusion system to a silicate melt which can then be quenched to recover the CO_2 content at the time of entrapment [*Cervantes and Wallace*, 2003; *Wallace et al*., 2015; *Hudgins et al*., 2015]. However, it is known that the temperature of homogenization in such experiments is significantly higher than the likely entrapment temperature, a mismatch which will cause the reconstructed relationship between CO_2 and major elements contents of the inclusion system to deviate from the natural case [*Sobolev and Danyushevsky*, 1994; *Massare et al*., 2002; *Wallace et al*., 2015; *Mironov et al*., 2015; *Schiavi et al*., 2016].

In this contribution, I first use a global compilation of observed melt inclusion compositions to assess the correspondence between calculated CO_2 saturation pressures and independent petrological and geophysical indicators of the likely depths of olivine growth and inclusion entrapment. I restrict this compilation to settings where the H_2O contents of the melts are relatively low and therefore have a negligible effect of the CO_2 saturation pressure estimates for the inclusions. This criterion restricts the study to mid-ocean ridge basalts (MORB), ocean island basalts (OIB), and a few samples from continental rift zones (CRZ), giving a data set with a 75th centile at 0.5 wt % H_2O. I then develop a model of the *P-V-T-X* evolution of olivine-hosted melt inclusions in water-free systems, and explore how the initial conditions of inclusion entrapment are reflected in the observed characteristics of the analyzed inclusion system. I confirm that bubbles formed upon cooling of the host are expected to sequester significant quantities of the inclusion CO_2 and find that the change in melt composition during crystallization plays a key role in bubble formation. However, barometry based on reconstructed inclusion compositions systematically underestimates the depth of inclusion entrapment when compared with independent barometric constraints. I conclude that decrepitation of melt inclusions, where the inclusion ruptures and loses CO_2 to the external melt, is the dominant process that controls the observed distribution of CO_2 in the compiled data set. Model results indicate, however, that when host olivines undergo substantial cooling intervals before eruption, the pressure decrease and bubble growth associated with the postentrapment crystallization may be sufficient to prevent decrepitation. In these rare cases, reconstruction of the inclusion composition may provide an accurate estimate of inclusion entrapment depth.

2. Barometric Inconsistencies: An Example From Iceland

The Eastern Volcanic Zone of Iceland has been the focus of a number of recent studies which have sought to better constrain the depth of magma chambers. A number of petrological approaches can be used to

estimate the pressures of crystal growth and melt inclusion entrapment in the magma chambers that feed the large fissure eruptions of this zone. The 1783 AD Laki eruption has been of particular interest [*Thordarson and Self*, 1993; *Guilbaud et al*., 2007; *Passmore et al*., 2012; *Neave et al*., 2013; *Hartley et al*., 2014]. The Laki samples carry macrocrysts of olivine, clinopyroxene, and plagioclase which record an interval of substantial cooling and crystallization in the crust. Large macrocrysts have core compositions that are significantly too primitive to be in equilibrium with the carrier liquid (Mg# = 44), with olivines ranging up to Fo_{87}, plagioclase to An_{89}, and clinopyroxene to Mg# of 84. Detailed microanalytical and textural studies have demonstrated that the melts which were trapped as melt inclusions in olivines were very similar to those which also crystallized to form clinopyroxene and plagioclase within the Laki plumbing system [*Neave et al*., 2013]. Parameterization of clinopyroxene-melt equilibria, based upon a version of the *Putirka* [2008] thermobarometer that has been corrected for systematic errors, was used to determine that the pressure of crystallization of the clinopyroxene was dominantly in the range 3–5 kbar [*Neave et al*., 2013], a range that is similar to the uncertainty on the barometer of $\pm$1.4 kbar. These depths of crystallization of clinopyroxene macrocrysts are consistent with more recent work on other large eruptions from the host system for Laki, Grímsvötn [*Neave et al*., 2015].

The Laki macrocrysts are carried to the surface by a liquid which is saturated in olivine, clinopyroxene, and plagioclase. These phases are present as relatively small phenocrysts within the groundmass glass of tephra samples, and these phenocrysts are close to chemical equilibrium with the carrier liquid with, for example, olivines at Fo_{72} [*Neave et al*., 2013]. The barometric method of *Yang et al*. [1996], which is based upon equilibrium between olivine, plagioclase, augite, and melt (OPAM), was then applied to the carrier liquid compositions. Clean tephra glasses were used as these liquid compositions, and found to provide estimates of a final equilibration pressure of 1–2 kbar [*Neave et al*., 2013]. Textural evidence indicates that this pressure estimate must be a hard minimum bound on the pressure of melt inclusion entrapment.

The CO_2 contents of olivine-hosted melt inclusions from Laki has recently been presented by *Hartley et al*. [2014], who measured both inclusion glass compositions and the density of the CO_2 vapor bubbles that were present in most of the inclusions. By combining their measurements of the major element compositions of the inclusion glasses with the CO_2 contents, it was possible to use the recent parameterization of CO_2 solubility from *Shishkina et al*. [2014] to determine an apparent saturation pressure, P_{sat}, for each melt inclusion. The results of this calculation are presented in Figure 1.

There is a striking inconsistency between the petrological barometers based on major element chemistry and those based on CO_2. The data set of *Hartley et al*. [2014] includes 116 inclusions, predominantly from the most forsteritic olivines in Laki but covering the full range in observed macrocryst and phenocryst compositions. Of these, 53 contained a bubble with measurable CO_2, 25 contained a bubble with CO_2 contents below the detection limit of the Raman spectroscopy and 38 contained no bubble. When saturation pressures were calculated using the CO_2 contents of the inclusion glasses alone, all of the pressures are less than that of the expected range of macrocryst growth, and about 90% are lower pressure than the final equilibration pressure of the major constituents of the carrier liquid. However, the textural evidence indicates that melt inclusion entrapment took place at the same pressure as the clinopyroxene grew.

Attempted reconstruction of the original inclusion composition by addition of the CO_2 measured in the bubbles back into the glass shifts the distribution of estimated P_{sat} to higher pressures. However, the fundamental inconsistency remains: half of the inclusions record P_{sat} which are less than the barometric constraints on the minimum carrier liquid equilibration pressure. Less than 10% of the reconstructed inclusions record P_{sat} that lie within the range expected from results of the clinopyroxene-liquid barometry and textural studies [*Neave et al*., 2013]. Bubbles matter, but perhaps not as much as had been hoped.

3. A Global Compilation of CO_2 Saturation Pressures in Basalts

The case study of Laki demonstrated an apparent inconsistency between estimates of magma storage depth derived from CO_2 and those based on independent petrological barometers. In order to establish the wider importance of such barometric mismatches, a global data set of olivine-hosted melt inclusions was built from the literature. The recent parameterization of CO_2 solubility in mafic melts by *Shishkina et al*. [2014] provides an accurate representation of the influence of both pressure and melt composition on solubility. Calculations of P_{sat} based on this parameterization are only likely to be effective for melts with

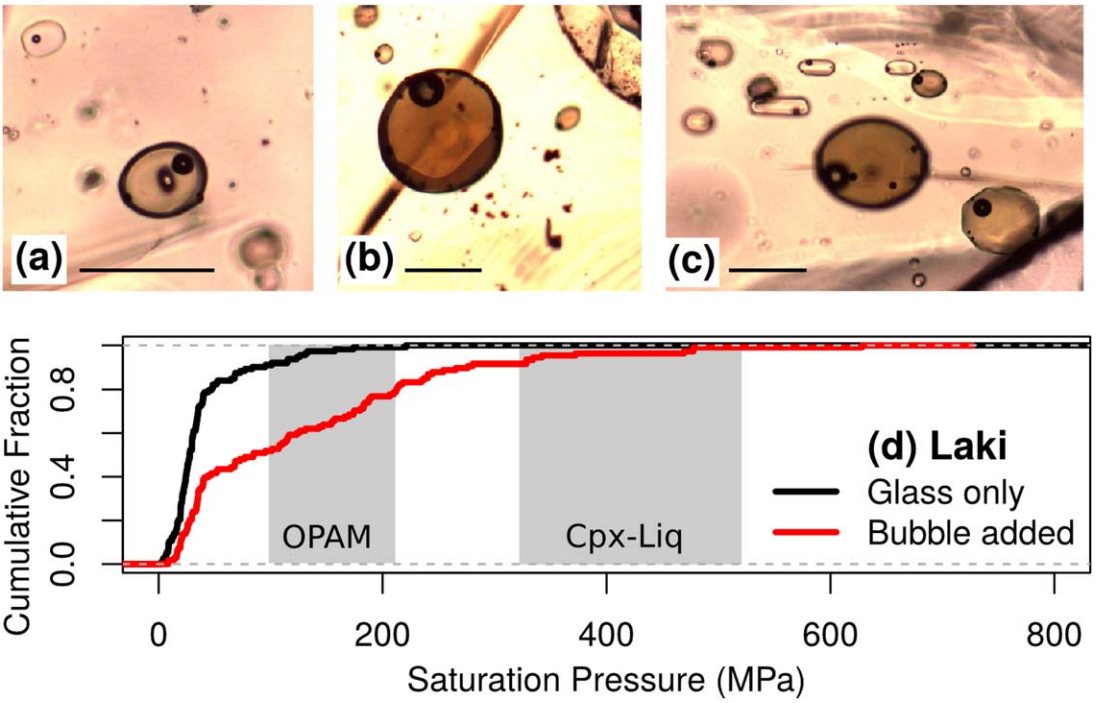

Figure 1. (a-c) Olivine-hosted melt inclusions from the study of Laki by *Hartley et al.* [2014]. Note the prevalence of inclusions hosting single vapor bubbles. In Figure 1a, the position of an ion-probe analysis pit can be seen in the central inclusion. (d) Saturation pressure estimates recovered from the Laki melt inclusion data set of *Hartley et al.* [2014] using the parameterization of *Shishkina et al.* [2014]. The P_{sat} is plotted as cumulative fraction of the 116 analyzed inclusions. The black line shows P_{sat} for melt with the CO_2 of the measured inclusion glasses. The red line shows that for the reconstructed inclusion compositions, where the measured bubble has been added back to the glass by calculation. Two inclusions, which had anomalously large vapor bubbles, of over 5% of the volume of the inclusion, were removed from this data set. The grey shaded fields show the pressure ranges of the clinopyroxene-liquid barometry and OPAM barometry described in the main text.

relatively low water contents. Joint CO_2-H_2O solubility models show that for a given melt CO_2 content, raising the melt H_2O increases the P_{sat} estimates. Limiting P_{sat} calculations to magmatic settings with relatively low water contents minimizes this systematic offset. The database therefore contains olivine-hosted melt inclusion analyses from mid-ocean ridge basalts (MORB), ocean island basalts and a few continental rift zone samples (CRZ). A large number of melt inclusion analyses are available from Iceland and these are therefore considered as a fourth category in the comparison of settings. The maximum H_2O of melt inclusions in the database is 2.1 wt %, which, given the CO_2 contents of those inclusions leads to a systematic underestimate in P_{sat} of less than 30 MPa. This effect is much less important for most of the data set: the median H_2O content of the inclusions is 0.26 wt %.

The quantity of volatile data from olivine-hosted melt inclusions has expanded enormously over the last decade, such that 2878 compositions were available in total. The data sources are provided in Table 1.

3.1. Comparison of Methods of Estimating Inclusion CO_2 at Entrapment

The individual data sets that were combined to generate the global compilation use different methods to estimate the CO_2 content of the inclusions at the time of entrapment, as described in section 1. The results of the P_{sat} calculations for these different methods are presented in Figure 2.

Table 1. Data Sources for Literature Compilation of Melt Inclusion CO_2 Contents

Setting	References
Mid-ocean ridges	*Saal et al.* [2002], *Colman et al.* [2015], and *Wanless and Shaw* [2012] *Wanless et al.* [2014, 2015]
Ocean islands	*Anderson and Brown* [1993], *Cabral et al.* [2014], and *Di Muro et al.* [2014] *Koleszar et al.* [2009], *Métrich et al.* [2014], *Sides et al.* [2014], and *Wallace et al.* [2015]
Iceland	*Hartley et al.* [2014] and *Neave et al.* [2014, 2015]
Continental settings	*Kamenetsky et al.* [2007] and *Head et al.* [2011] *Hudgins et al.* [2015] and *Oppenheimer et al.* [2011]

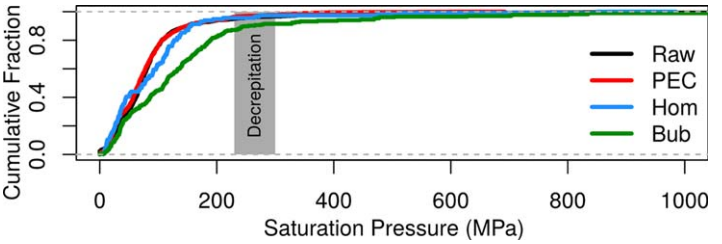

Figure 2. Cumulative distribution functions for the calculated P_{sat} in the data set, subdivided according to the method of reconstruction of the inclusion composition at the time of entrapment. The black line, "Raw," refers to inclusions that have had no correction applied ($n = 1342$). The red line, "PEC," is for inclusions that have had standard postentrapment crystallization corrections applied to their compositions ($n = 868$). The blue line, "Hom," refers to inclusions that have been experimentally heated with the aim of rehomogenization of any bubbles into the melt inclusion ($n = 205$). The green line, "Bub," shows inclusions where the estimated CO_2 content of any bubble has been added back into the measured glass by calculation ($n = 515$). The grey shaded area shows the likely range of pressure differences between inclusion and exterior required to decrepitate the inclusion [*Wanamaker et al*., 1990; *Campione et al*., 2015].

The different methods of reconstruction of initial melt inclusion compositions provide remarkably similar distributions of P_{sat}: The cumulative distribution curves for uncorrected inclusions, inclusions with postentrapment crystallization corrections and experimentally heated inclusions are almost coincident. The 90th percentile for these three distributions lies at 149, 148, and 154 MPa, respectively, with an almost uniform distribution of points to lower pressure. The distribution of P_{sat} for inclusions where the correction involves bubble addition look slightly different with a 90th percentile at 250 MPa and a longer tail out to higher pressures. About 10% of the bubble-corrected inclusions record P_{sat} that is higher than the decrepitation threshold for large inclusions in olivine suggested by *Wanamaker et al*. [1990], as described later in the text.

3.2. Comparison of Settings

The cumulative distribution curves of P_{sat} for subgroups of the global data set according to magmatic setting are shown in Figure 3. The distribution of observed CO_2 contents in each setting is also shown in this figure, and demonstrates that all settings preserve a large range of inclusion compositions. While 90% of the inclusions in the data set contain less than 1178 ppm CO_2, a long tail is present in the distribution for each setting from about 1000 ppm up to 3000 ppm. The distributions for ocean islands and continental volcanics are offset to slightly higher CO_2 contents than those of the MORB and Iceland distributions. The similarity of the MORB and Iceland distributions should be noted.

The inclusion CO_2 contents were converted into P_{sat} using the major element compositions of the inclusions and the solubility parameterization of *Shishkina et al*. [2014]. This conversion brings the distribution curves from each setting closer together for P_{sat} than was observed in the CO_2 plot. The cause of this shift is that the compositional parameterization includes terms such that the CO_2 solubility is increased with increasing alkali contents in the melt and decreasing silica. Therefore, the higher alkali contents and low silica contents of OIB and CRZ mafic volcanics leads to higher CO_2 solubility at fixed pressure, squeezing the OIB and CRZ distributions of P_{sat} to lower pressures.

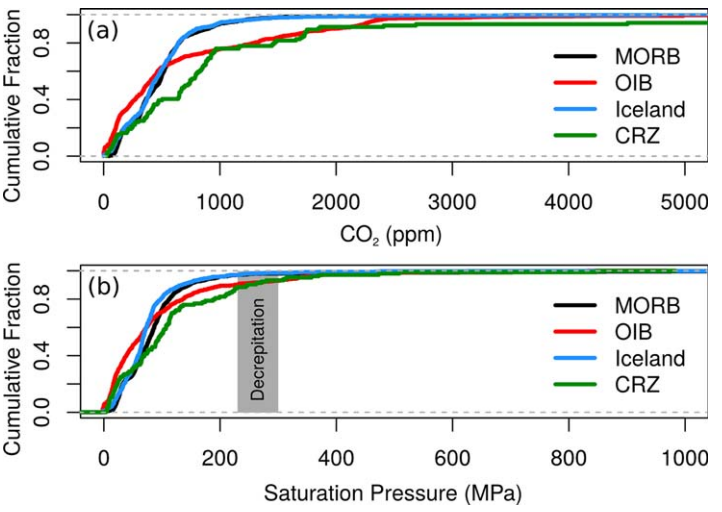

Figure 3. (a) Cumulative distribution functions for the observed and reconstructed CO_2 content of olivine-hosted melt inclusions according to magmatic setting: mid-ocean ridges (MORB, $n = 1003$); ocean islands (OIB, $n = 843$); Iceland ($n = 849$); continental rift zones (CRZ, $n = 170$). (b) Cumulative distribution functions for the calculated P_{sat} in the data set, subdivided according to the magmatic settings. The range of expected inclusion decrepitation pressures is shown as a grey box.

The result of taking the compositional dependence of solubility into account reveals the striking similarity of saturation pressures in each setting. These similarities are at first surprising. If the CO_2 contents of melt

inclusions carry a record of depths of magma storage, then these distributions would be expected to vary significantly between settings. Variations in lithospheric thickness, crustal thickness, and melt supply rate are all expected to influence the depth distribution of magma chambers [*McKenzie and Bickle*, 1988; *Morgan and Chen*, 1993; *Annen and Sparks*, 2002; *Geist et al*., 2014]. Thick lithosphere is likely to be related to deeper crystallization of rising mantle melts. Many of the samples in the OIB suite are from ocean islands such as Hawaii, where lithosphere of 90 km or more is present. Similarly thick lithosphere may be found in continental settings. Nevertheless, the distribution of P_{sat} from these settings is very similar to MORB, where the lithospheric thickness is generally less than 90 km. Crustal thickness has long been thought to influence the depth distribution of magma storage because there is a substantial density shift at the Moho. While Iceland has an average crustal thickness of ~30 km, typical MOR crustal thickness is less than ~10 km. However, this variation in crustal thickness and the likely control on the depth of magma storage is not reflected in the saturation pressures of CO_2 in melt inclusions from these settings: MORB and Iceland have barely distinguishable distributions of P_{sat}.

3.3. Might Decrepitation Control the P_{sat} Distribution?

The similarity of the distributions of P_{sat} from differing magmatic settings is a surprise. While the mass and thermal budget of these settings differ markedly and should correspond to varying distributions of magma storage depth, the distribution of the CO_2 content of melt inclusions appears to be insensitive to such fundamental variations. Taken together with the summary of observations from the Laki eruption presented in the previous section, this evidence indicates that the CO_2 contents of olivine-hosted melt inclusions do not provide accurate barometric constraints on the depth of magma chambers in basaltic settings.

The observed melt inclusion P_{sat} do not record their entrapment pressures in straightforward fashion and it is therefore important to explore the processes that control this mismatch. The methods that have been used to correct observed melt inclusion composition for postentrapment processes are clearly failing to reconstruct the original CO_2 composition in most cases. One processes that is not possible to correct for, because it involves irreversible loss of mass, is decrepitation of the inclusion. An experimental study of the decrepitation of CO_2 fluid inclusions in San Carlos olivine at magmatic temperatures found an apparent relationship between inclusion radius and the pressure retained in the inclusions during the experiment [*Wanamaker et al*., 1990]. For inclusions with a radius of $>10\,\mu$m, the maximum pressure difference between the inclusion and the exterior that can be maintained with decrepitation is 220 MPa. The propensity for smaller inclusions to avoid decrepitation is well known from the study of fluid inclusions [*Bodnar and Bethke*, 1984]. These observations have recently been further modeled by *Campione et al*. [2015]. Their calculations indicate that smaller inclusions, with diameters of $<10\,\mu$m, may retain higher pressure differences between inclusion and host before decrepitation. In addition to these models, it has long been understood that observations of melt-filled cracks and haloes of tiny inclusions around large inclusions may indicate a role for decrepitation in the evolution of olivine-hosted inclusions [*Roedder*, 1965; *Portnyagin et al*., 2005].

It is notable that the observed distributions of inclusion P_{sat} from CO_2 measurements are dominated by pressures lower than the experimental decrepitation pressure of olivine-hosted fluid inclusions (Figures 2 and 3). Furthermore, all of the cumulative distributions show a change in gradient over a pressure interval between the decrepitation pressure and about 130 MPa. These observations indicate that decrepitation of olivine-hosted melt inclusions can account for the mismatch between the observed distribution of P_{sat} and the results of independent petrological barometers, for example, at Laki, and for the lack of sensitivity of this distribution to fundamental variations in the magmatic setting. Further evidence for the role of decrepitation comes from rare cases where both fluid inclusions and melt inclusions from a single suite of olivines have been examined for their CO_2 contents. These studies find that the small fluid inclusions preserve systematically higher pressures than the larger melt inclusions [*Métrich et al*., 2014].

In order to determine whether decrepitation is likely to occur for inclusions that are trapped at pressures of ~250 MPa, it is necessary to have a method for tracking the evolution of the pressure difference between the inclusion and the external melt during the transit from the entrapment depth to eventual eruption. Postentrapment processes are known to reduce the pressure in the inclusion [*Roedder*, 1984; *Steele-Macinnis et al*., 2011; *Bucholz et al*., 2013] and may help inclusions to avoid decrepitation. The following section therefore contains a description of the development of a model that can be used to assess the possible

importance of decrepitation and more generally to understand how the observed final distribution of CO_2 P_{sat} reflects the initial distribution of entrapment conditions.

4. A Model of *P-V-T-X* Evolution in Olivine-Hosted Melt Inclusions

The observed compositions of olivine-hosted melt inclusions contain information about the conditions of entrapment but are also substantially overprinted by postentrapment processes. It is therefore desirable to have a model that can be used to predict how such processes influence inclusion compositions. A number of thermomechanical models of host-inclusion systems have previously been developed and applied to olivine-hosted melt inclusions in nature [*Tait*, 1992; *Zhang*, 1998; *Wallace et al*., 2015] and also to understand the behavior observed during experimental heating [*Schiavi et al*., 2016]. The goal of the model described below was to examine how the initial composition of the inclusion is modified as the olivine host travels through a specified *P-T* path. This problem is similar to one described for inclusion-host systems traveling through externally imposed *P-T* paths in metamorphic rocks by *Guiraud and Powell* [2006].

This general model was designed to incorporate two postentrapment effects that have previously been proposed to influence inclusion pressure. The first is the effect of differential contraction of the host and inclusion on cooling [*Roedder*, 1984; *Lowenstern*, 1995]. The second is the role of crystallizing a phase with different density to the melt on the inclusion walls [*Steele-Macinnis et al*., 2011; *Sides et al*., 2014]. The model also includes a third effect that is found to be important. As the melt inclusion major element composition changes during olivine crystallization, this influences the solubility of CO_2 in the melt. According to the solubility model of *Shishkina et al*. [2014] the removal of olivine from the melt composition can significantly lower CO_2 solubility and even at fixed inclusion pressure can lead to CO_2 saturation.

In order to ensure efficient model development and to provide flexibility to explore a range of host *P-T* paths, it was necessary to make a number of simplifications. The model was only run for olivine, although it could, in principle, be extended to other phases. Only CO_2 was included in the models of the solubility of volatiles in the silicate melt and the equation of state of the fluid. However, the role of H_2O on the equilibrium between silicates was incorporated in the model. The model results are suitable for comparison with the global compilation of olivine-hosted melt inclusions in low H_2O systems that was presented in the previous section. The irreversible effects of diffusion and host plasticity [*Schiavi et al*., 2016] were not included in the model, with the exception of diffusive controls on CO_2 transfer between melt and bubble during eruptive quenching of the system. The diffusion of H_2O may play a role in the formation of vapor bubbles in inclusions, but this effect is not thought to be important in H_2O-poor systems such as MORB and OIB [*Bucholz et al*., 2013].

4.1. Defining a *P-T-(t)* Path for the Host Crystal

The *P-T-(t)* path of the host crystal for the inclusion of interest was specified by first setting the entrapment conditions and then adding segments to the *P-T* path. The time aspect, *t*, is only considered during the final eruptive quenching of the system. The *P-T* segments were defined to simulate isobaric cooling in a magma body at fixed depth, adiabatic decompression during melt ascent or quenching after eruption. The models are flexible so that any number of segments of isobaric cooling and adiabatic decompression can be added. All that is required is an input of the temperature drop for cooling or the target final pressure for the decompression.

4.1.1. Conditions of Inclusion Entrapment: Initial *P-T-X*

An initial melt composition, *X*, needs to be specified as input to the programme. This composition was chosen to generate plausible parental melts for each of the eruptions to be studied. The initial melt composition should have a Mg# that is in equilibrium with the olivine host of the melt inclusion of interest. The programme PETROLOG [*Danyushevsky and Plechov*, 2011] was used to backward correct high Mg# matrix glass compositions or plagioclase hosted-melt inclusion compositions for the effect of fractional crystallization. It was assumed that the relationship between the observed matrix glass composition and the parental melt was dominated by olivine crystallization, using the parameterization of olivine-liquid equilibrium from *Beattie* [1993]. The assumption of olivine control is not correct in detail, because some Icelandic eruptions are known to carry high Mg# clinopyroxene and high An plagioclase that have crystallized at high temperature along with Fo_{89-90} olivines [*Maclennan et al*., 2003; *Winpenny and Maclennan*, 2011, 2014]. Furthermore,

many of these olivines host melt inclusions with highly variable trace element and isotopic compositions [*Gurenko and Chaussidon*, 1995; *Maclennan*, 2008a, 2008b], indicating that melt inclusions and their carrier liquids are related by concurrent mixing and crystallization rather than evolution along a single liquid line of descent. Nevertheless, the choice of an initial parental liquid by backward correction to equilibrium with a fixed olivine composition allows us to investigate the effects of postentrapment crystallization for individual inclusions. The oxygen fugacity of the system was fixed in the PETROLOG correction models with reference to the QFM buffer. These corrections were also carried out at a model pressure that was fixed in order to match the desired inclusion entrapment conditions. Elemental partitioning between olivine and liquid is thought to be relatively insensitive to pressure, so this model pressure has little influence on the calculation of the parental melt composition.

The H_2O and CO_2 contents of the parental melts were also specified. The H_2O contents of the parental melts can be estimated using the measured H_2O in the melt inclusions. The H_2O of the observed inclusions in the Icelandic suites has been influenced by diffusive homogenization at pressures greater than those expected for significant H_2O loss to a vapor phase [*Hartley et al*., 2015]. Therefore, the observed inclusion H_2O provides an estimate of the carrier liquid H_2O during storage at depth and was input to the PETROLOG correction models. The CO_2 contents of the initial liquids were defined at a number of different values because one of the goals of this modeling approach was to explore the relationship between melt CO_2 contents at entrapment and the final composition of the inclusion glass and vapor bubble.

The results for Icelandic Eastern Volcanic Zone eruptions, such as Laki, are based on models where the initial CO_2 was typically to match the maximum observed in any of the inclusion glasses (1232 ppm). However, the models are flexible enough to be able to simulate entrapment at differing levels of supersaturation or undersaturation in CO_2 at the chosen pressure of entrapment.

After the initial melt composition and pressure had been fixed in the model, the temperature of olivine saturation in the liquid was calculated using pressure and the MgO content of the melt with the model of *Sugawara* [2000]. This approach allows us to ensure that the melt to be included is saturated in olivine at the conditions of entrapment. The ferric iron content of the melt at these conditions was then obtained by setting the oxygen fugacity relative to the QFM buffer and using the model of *Kress and Carmichael* [1991]. This repartitioning of ferric and ferrous iron has a small effect on the MgO content of the liquid in terms of wt % oxides, so an iterative approach was used to determine the saturation temperature and ferric iron content of the melt at entrapment. The host olivine composition was set to be in equilibrium with this initial liquid using the parameterization of *Beattie* [1993].

4.1.2. Isobaric Cooling

A common feature of basalts from mid-ocean ridge and ocean island settings is that the composition of olivine macrocrysts is too forsteritic to be in equilibrium with the liquid that carries them to the surface for eruption [*Garcia*, 2000; *Thomson and Maclennan*, 2013] and it is likely that substantial cooling, of 100°C or more, occurs between inclusion entrapment and the final ascent of the carrier melt prior to eruption. While barometry of basaltic systems remains imprecise, observations from Iceland indicate that substantial cooling and melt evolution can occur over limited ranges in pressure [*Winpenny and Maclennan*, 2011]. Such evolution is therefore modeled using intervals of isobaric cooling.

4.1.3. Adiabatic Decompression

If melt rises quickly toward the surface and loses little heat to the surroundings then its P-T path will roughly follow that of the adiabat of the host liquid. The adiabatic gradient was calculated using the standard expression [e.g., *McKenzie and Bickle*, 1988]. The specific heat capacity was calculated using the host liquid composition and the method of *Lange and Navrotsky* [1992] and the density and thermal expansion coefficient from *Lange and Carmichael* [1990]. In practice, the cooling during adiabatic decompression is small, corresponding to $\sim 4\,^{\circ}\mathrm{C\,kbar^{-1}}$.

The subsurface *P-T* path of the host crystal and its carrier liquid was specified by adding segments of isobaric cooling and adiabatic decompression. The final conditions of storage were chosen in order to match those thought to be appropriate for the generation of the carrier liquid composition as based on available thermobarometric estimates. The substantial uncertainties associated with such estimates indicate that a range of storage and ascent models should be explored for each eruption, to see how these variations in *P-T* path may be expressed in the CO_2 budget of the melt inclusions.

4.1.4. Quenching

It has been established that the final parts of the near-surface cooling history of melt inclusions and their olivine hosts can have an important influence on their volatile element contents, particularly H_2O [*Gaetani et al*., 2012; *Lloyd et al*., 2013]. This phase of eruptive quenching at atmospheric pressure was modeled in order to establish its role in the formation and evolution of CO_2-rich vapor bubbles in the inclusions. It was assumed that no major-element exchange by diffusion or crystallization occurred in the inclusion-host system during this quench. In contrast, diffusive exchange of CO_2 between the melt inclusion and vapor bubble was allowed under certain circumstances, and the pressure-volume evolution of the inclusion system was tracked during quenching. The presence of vapor bubbles with varying CO_2 density according to the nature of posteruptive cooling indicates that the quench interval may play an important role in controlling bubble volume and density and therefore must be modeled [*Hartley et al*., 2014; *Neave et al*., 2014]. The inclusions examined in this paper are from samples with a variety of cooling rates: from clean, glassy pillow rims, and tephra glass through to partially glassy crusts on the exterior of flow-lobes. Estimates of cooling rate during these quenches to glass come from the studies by *Gottsmann et al*. [2004] of Hawaiian pahoehoe crusts (0.1–2 $K\,s^{-1}$) and *Nichols et al*. [2009] of pillow lavas (2–50 $K\,s^{-1}$). For Laki lava samples, it is also useful to consider a much slower cooling interval during days of residence in flowing lava prior to quench in pahoehoe lobes, perhaps of as little as 3×10^{-6} $K\,s^{-1}$. This slow cooling can also be modeled by an isobaric cooling interval using the technique described in the previous subsection.

The cooling was modeled by setting a value for dT/dt between the temperature of eruption, T_m, and the glass transition temperature for the inclusion, T_g. Below the glass transition temperature, it is assumed that the rheology of the inclusion switches so that no further volume change of the bubble can occur.

The glass transition temperature was calculated from the relationship between viscosity at T_g and cooling rate [*Dingwell and Webb*, 1990; *Gottsmann et al*., 2004] and estimates of melt viscosity from the parameterization of *Giordano et al*. [2008]. The calculated T_g vary from about 600°C to 750°C.

Partitioning of CO_2 between the melt inclusion and vapor bubble is limited by diffusion through the melt over this cooling interval. While there is relatively little experimental data to constrain CO_2 diffusion in basaltic melt, a working parameterization was provided in the review of *Ni and Keppler* [2013]. A rough approximation of the effect of diffusion-limited exchange was incorporated into the models by estimating an effective closure temperature, T_c, for CO_2 in the melt inclusion, using the expressions of *Dodson* [1973]. The higher the specified cooling rate, the higher the apparent closure temperature. The range of inclusion sizes for the data considered in this paper ranges from about 15 to 100 μm radius, with the lower limited imposed by the spatial resolution of standard SIMS analyses. At temperatures above T_c during the model quench, it is assumed that the vapor bubble and melt inclusion can reach equilibrium according to the CO_2 solubility laws of *Shishkina et al*. [2014], while at lower temperatures the mass of CO_2 in the bubble and melt remain fixed.

4.2. Calculation of *P-T-(t)* Path for Inclusion

We follow the approach of *Zhang* [1998] and *Guiraud and Powell* [2006] and model the pressure evolution of inclusions that are small compared to their host using

$$\left(\frac{V_h(P,T)}{V_h(P_0,T_0)}\right)=\left(\frac{V_i(P_i,T)}{V_i(P_0,T_0)}\right)-\frac{3}{4G}(P_i-P), \tag{1}$$

where V_h is the volume of the host, V_i is the volume of the inclusion, P and T are pressure and temperature, with the subscript 0 referring to the entrapment conditions and the subscript i referring to the inclusion. The shear modulus, G, of the olivine host is set at 90 GPa for the calculations shown below [*Núñez-Valdez et al*., 2010]. This simple expression provides a good first step for exploring the effects of postentrapment processes on the evolution of olivine-hosted inclusions. However, if inclusions are large, have complex geometries, are situated close to the crystal edge or are situated in a strongly anistropic host then a finite element approach modeling may be required.

Calculation of the relative volume change of the olivine host along the specified *P-T* path, the left-hand term in equation (1) is straightforward. The Tait-Equation-of-State (TEOS) for olivine from *Holland and Powell* [2011] was used for this purpose. In order to ensure stability of solution, equation (1) was solved for P_i using a numerical bisection method. While the initial volume of the inclusion, $V_i(P_0,T_0)$, is easy to calculate, the

volume of the inclusion system varies in more complicated fashion due to the possibility of crystallization of olivine on the inclusion walls and the exsolution of a CO_2 rich vapor or fluid phase from the melt.

4.2.1. Postentrapment Crystallization

Postentrapment crystallization (PEC) of olivine-hosted melt inclusions that are found in glassy or even partially glassy groundmass matrices is typically controlled by olivine crystallization on the inclusion rim. The extent of postentrapment crystallization was estimated using the relationship between melt MgO content and temperature for olivine-saturated basaltic liquids proposed by [*Sugawara*, 2000]. As the host olivine moves along its specified *P-T* path, the temperature in the inclusion is assumed to remain the same as that of the host, allowing the inclusion MgO content to be calculated. The difference between this MgO and the initial MgO of the entrapped melt is controlled by olivine crystallization on the walls. Using the stoichiometry of olivine and a simple parameterization of the partitioning of Fe and Mg between olivine and melt it is then possible to calculate the fraction of PEC, the olivine composition, and the melt composition. This approach assumed equilibrium between the all of the PEC olivine and the melt, which simplifies calculation of the physical properties of the PEC olivine. These calculations were first performed using the parameterization of elemental partitioning between olivine and melt from [*Beattie*, 1993], which involved an iterative solution that was computationally costly and was sometimes unstable. An alternative approach, which used a $K_d^{Fe-Mg}=0.3$ was used to improve the initial guesses for the iterative solution, was found to agree to within a couple of percent PEC with the more complete parameterization. This simpler approach was used to speed up calculation. The model, at this stage, does not include the effect of diffusive re-equilibration of Mg and Fe between the host olivine, the growing PEC rim, and the melt. In order to include these effects, more information about the temporal evolution of temperature in the subsurface plumbing system would have to be supplied. The composition of the PEC olivine rim and the melt in the inclusion was therefore known as a function of temperature. It was assumed that ferric iron did not enter the olivine, meaning that the proportion of ferric iron to total iron increased during PEC. The CO_2 content of the inclusion was corrected to account for PEC.

4.2.2. Exsolution of a CO_2-Rich Fluid Phase

The concentration of CO_2 in the melt in the absence of bubble exsolution was corrected for PEC as described above. The model of *Shishkina et al*. [2014] was used to determine the solubility of CO_2 in the melt inclusion, once the melt inclusion composition had been corrected for olivine PEC. This parameterization is sensitive not only to the pressure of the melt, but also the major element composition, as shown in Figures 4–6. The effect of increasing extents of olivine PEC is to substantially decrease the CO_2 solubility. If the calculated CO_2 solubility is less than the CO_2 in the PEC-corrected melt composition, then a CO_2-rich bubble must form. The relative mass of the CO_2 bubble and the remaining melt can be estimated from the difference between CO_2 solubility in the melt and the PEC corrected CO_2.

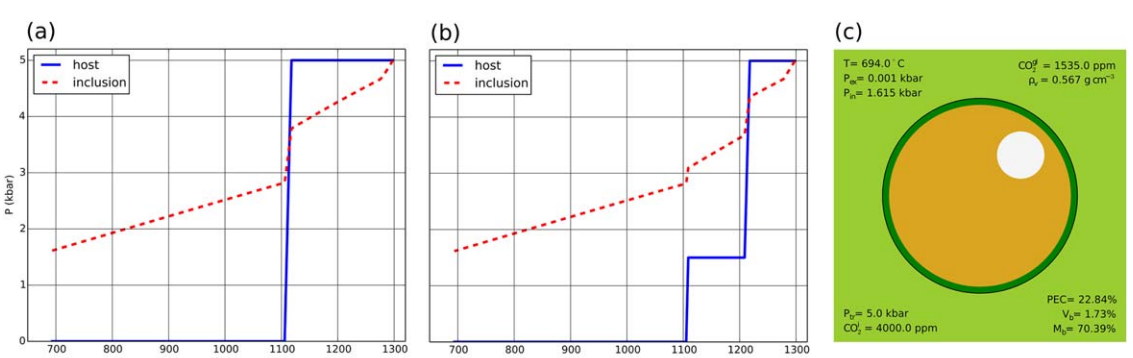

Figure 4. Animated versions of similar material can be found in supporting information movies S1–S3. *P-T* paths for host and inclusion. The blue line shows the imposed host path, and the red dotted line the calculated resultant path for the inclusion. (a) Laki model with single decompression step between deep storage and eruption. More details provided in text. (b) Two-stage model, with isobaric cooling intervals in chambers at two depths. (c) Final conditions of melt inclusion system, calculated at the glass transition temperature, plotted to mimic appearance of an olivine-hosted melt inclusion under a petrographic microscope. Bright green is the original olivine host and dark green is olivine grown on the inclusion walls during postentrapment crystallization. The mass percent of such crystallization is shown as "PEC." The white circle represents the bubble, which has a relative volume given by V_b and contains a mass fraction M_b of the initial CO_2 in the trapped inclusion. The inclusion and bubble are assumed to be spherical and sliced through their centers for the plotting, so that their cross-sectional areas can be simply related to the volumes. The initial entrapment pressure, P_{tr}, and the initial CO_2 content of the inclusion, CO_2^i are shown in the bottom left. The final conditions at the glass transition temperature are shown at the top left, with P_{ex} being the external pressure and P_{in} the inclusion pressure. The top right shows the compositional properties that can be analyzed in the system: the final CO_2 content of the glass and the density of the bubble.

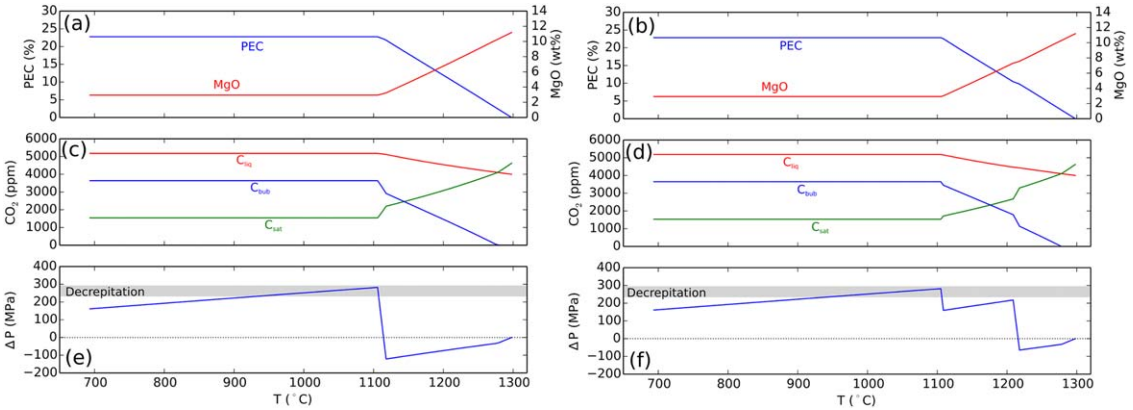

Figure 5. Evolution of selected properties of the inclusion system for the model *P-T* paths shown in Figure 4, plotted against imposed external temperature. Figures 5a, 5c, and 5e correspond to the single decompression model and Figures 5b, 5d, and 5f to the two-stage model. (a, b) The extent of postentrapment crystallization, PEC, and the MgO content of the melt inclusion. (c, d) The evolution of the CO_2 in the system. C_{liq} shows the predicted variation in the CO_2 of the melt in the absence of bubble formation: this tracks the enrichment of incompatible elements in the melt during PEC. C_{sat} is the calculated CO_2 solubility in the melt. When C_{sat} is less than C_{liq} then a bubble forms. The quantity of CO_2 in the bubble is expressed as C_{bub}, which records the effect on the melt concentration if the bubble CO_2 was returned back to the melt. (e, f) The pressure difference between the inclusion and the exterior of the olivine is plotted as ΔP. Decrepitation pressures are shown as a grey band.

4.2.3. Melt Inclusion System Volume

The melt inclusion system volume was calculated as a function of P and T using the relative masses of PEC, bubble, and melt from above and the relevant expressions for volume/density for the melt from *Lange and Carmichael* [1990] and *Ochs and Lange* [1999], for the olivine from *Holland and Powell* [2011] and for the CO_2 from the Compensated-Redlich-Kwong equation of state from *Holland and Powell* [1991]. This approach was used to calculate the V_i terms in equation (1). This equation was then solved for P_i, allowing the *P-T* path of the inclusion to be calculated along with a number of physical and chemical properties of the melt inclusion system.

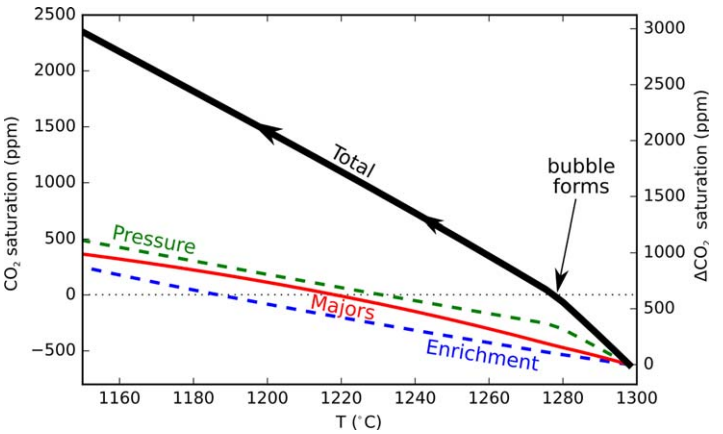

Figure 6. Evolution of CO_2 saturation during postentrapment crystallization in melt inclusion hosted by olivine following the *P-T* paths from Figure 4a. The left-hand axis shows the scale for CO_2 saturation in the melt inclusion. At the point of entrapment, at high temperature, the inclusion is slightly undersaturated in CO_2, giving negative values on this scale. The solid black line shows the total saturation: a bubble is predicted to form at about 1280°C and grow on further cooling. The right-hand scale shows the variation in saturation referenced to the initial conditions of entrapment. The green dashed line shows the role of pressure change alone in controlling the change in saturation. The blue dashed line shows the effect of enrichment of CO_2 in the melt inclusion by PEC. The red line shows the influence of the changing major element composition of the inclusion during PEC on the predicted solubility.

5. Model Results

5.1. Models Based on the Laki-Grímsvötn System

The results of two models, roughly based upon observations from the Laki-Grímsvötn system, are shown in Figures 4 and 5. The initial entrapment conditions at 500 MPa were based upon previous thermobarometric studies of this system [*Neave et al.*, 2013, 2015]. The major element content of the initial trapped melt was based upon the composition of primitive plagioclase-hosted melt inclusions from the Saksunarvatn tephra, an early Holocene product of the Grímsvötn system [*Neave et al.*, 2015]. This melt is in equilibrium with olivine with a forsterite content of 87 mol % (Fo_{87}), similar to some of the most forsteritic cores found in

Laki macrocrysts [*Neave et al*., 2013; *Hartley et al*., 2014]. The olivine liquidus for this melt at 500 MPa is 1298°C. An initial melt CO_2 content of 4000 ppm was chosen because this value is close to the expected mean parental Laki melt based on CO_2-Nb systematics [*Hartley et al*., 2014]. These melts are close to CO_2 saturation at 500 MPa.

In the model shown in Figure 4a the melt goes through an isobaric cooling interval of 180°C before adiabatic decompression toward the surface. In contrast, Figure 4b shows the results of a model where 80°C of cooling occurs in the deep chamber, before decompression to a chamber at 150 MPa. A further 100°C occurs in this shallow body prior to eruption. This two-stage storage model is designed to simulate the *P-T* path for typical Laki–Grímsvötn eruptions from previous petrological studies [*Neave et al*., 2013, 2015].

The information provided in Figures 4 and 5 show a selection of the calculated properties of the inclusion system along the imposed *P-T* paths. The cooling path is shown from the initial entrapment conditions through to the point at which the glass transition temperature is reached. The evolution of the inclusion system during posteruptive cooling at low external pressure can have important effects in the final volume and density of the bubbles, but these variations are not explored here, and instead a rapid quenching rate of 10 K s^{-1} was used for all the models.

A number of important effects are observed in the subsurface part of the path. First, it is clear that postentrapment crystallization plays an important role in lowering inclusion pressure. The final pressure in the inclusion system is substantially lower than that of entrapment. The change in the slope of the inclusion *P-T* path at about 1280°C in these models is caused by the formation and growth of the bubble at the lower pressures caused by increasing extents of postentrpament cooling. Figures 5e and 5f show that while PEC initially causes underpressure of ~100 MPa in the inclusion, the pressure difference between the exterior and inclusion increases significantly during pre-eruptive decompression. The peak pressure difference between the inclusion and exterior occurs at the point of eruption and in these models, this pressure difference reaches 280 MPa. In nature, such pressure differences may lead to decrepitation of the inclusions.

While the models in Figures 4a and 4b follow differing *P-T* paths, the initial conditions and the final *P-T* are the same. Because the features included in these models are reversible, the final system state is independent of the path. However, it should be noted that differences in the path are significant. For example, the inclusion overpressure is closer to the decrepitation limit for a greater temperature interval in Figure 5e than in Figure 5f.

The distribution of CO_2 in the inclusion system changes substantially as the host olivine follows the specified *P-T* paths (Figures 5c and 5d). The predictions of these particular model runs are that over 70% of the original mass of carbon is transferred to the bubble. The final glass CO_2 content of 1535 ppm corresponds to a calculated saturation pressure of 290 MPa, much less than the entrapment pressure of 500 MPa.

While the main focus of this manuscript is the pre-eruptive behavior of the system, it is worth noting that in the models shown in Figure 4, the rapid quench leads to the inclusions following a P-T path that is very similar to that predicted for the pure CO_2 isochore in the bubbles. Furthermore, the relatively high density of the CO_2 in the bubble at the end of the model path is such that if this bubble were to be viewed under STP conditions then the CO_2 would be present as a two-phase mixture of vapor and liquid. If such phase separation is not taken into account in, for example, Raman measurements of the bubble composition, then reconstructed inclusion compositions will be systematically low in CO_2.

5.2. Why Does Postentrapment Crystallization Cause Bubble Growth?

It has previously been suggested that pressure changes in an inclusion caused by cooling can lead to exsolution of a vapor bubble [*Roedder*, 1984; *Lowenstern*, 1995]. The pressure variations are driven by differential contraction of host and inclusion and by the density difference between melt and the olivine that grows during postentrapment crystallization [*Steele-Macinnis et al*., 2011]. Enrichment of the melt inclusion in incompatible elements during PEC can also raise the CO_2 content of the melt toward that of saturation.

The causes of varying CO_2 saturation in the system can be examined using the model results. A short part of the postentrapment cooling path from the model of Figure 4a is shown in detail in Figure 6, focusing on the evolution of CO_2 saturation in the system. These results show that the pressure drop and enrichment of CO_2 during postentrapment crystallization contribute almost equally to the increased saturation of CO_2 in the system and therefore the nucleation and growth of bubbles. A third effect which has not previously

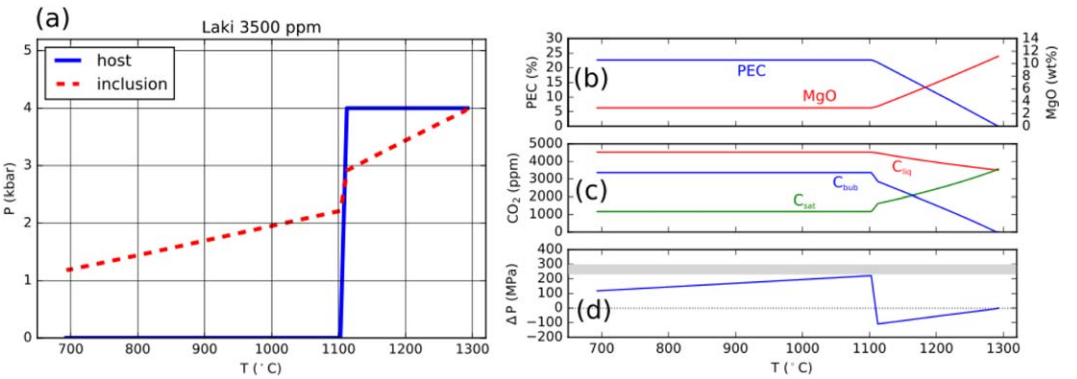

Figure 7. Model result for Laki model parental melt with entrapment pressure of 4 kbar and initial CO_2 of 3500 ppm. (a) Imposed host and calculated inclusion *P-T* paths, as for Figure 4a. (b) Selected model inclusion properties, for comparison with Figure 5.

been recognized plays an equally important role in controlling CO_2 saturation during postentrapment evolution. As the crystallization proceeds, the major element composition of the melt inclusion varies (e.g., Figure 5a). The solubility of CO_2 is a function of melt composition as well as pressure, and the parameterization of *Shishkina et al*. [2014] shows that during olivine crystallization the solubility CO_2 can drop substantially. This important effect needs to be included in models of postentrapment evolution of volatiles in melt inclusions.

5.3. *P-T* Paths, Entrapment Conditions, and Decrepitation

5.3.1. Varying Entrapment Pressure

Lower entrapment pressure reduces the maximum pressure difference between the inclusion and the exterior, therefore minimizing the likelihood of decrepitation. The results of the model shown in Figure 7 demonstrate this effect in quantitative terms. The maximum pressure difference between the inclusion and the exterior in this model is 220 MPa, just beneath the lower limit for decrepitation (Figure 7d). If this inclusion can avoid decrepitation, then reconstruction of the original composition by adding bubble composition to glasses may be able to recover information about the depth of entrapment.

5.3.2. Varying Entrapment Temperature

At a given pressure, the model entrapment temperature is lower for melts with more evolved compositions. Therefore, it is not possible to independently vary entrapment temperature and melt major element composition in the model. The calculated inclusion composition for a temperature of 1160°C was taken from the model shown in Figure 4a and then used as the starting composition for a model where entrapment takes place at lower temperature (Figure 8). The starting composition was fixed to contain 3300 ppm CO_2, a value that is just undersaturated at 500 MPa for the melt major element composition. The forsterite content of the olivine host would be 80 mol % in this case.

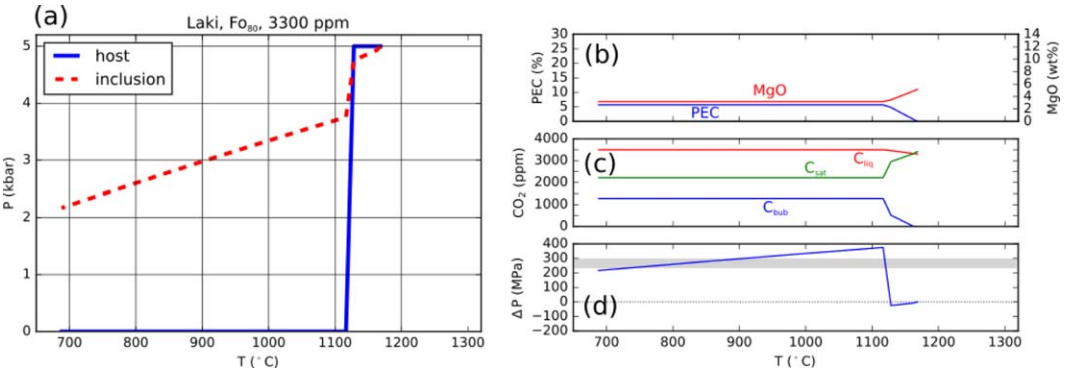

Figure 8. Model result for Laki model parental melt with entrapment temperature of 1160°C and initial CO_2 of 3300 ppm. (a) Imposed host and calculated inclusion *P-T* paths, as for Figure 4a. (b) Selected model inclusion properties, for comparison with Figure 5.

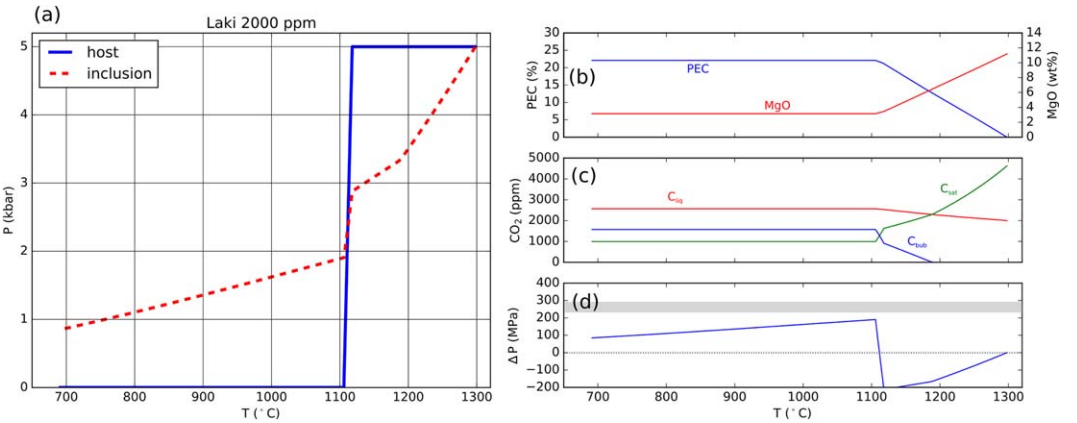

Figure 9. Identical model settings to Figure 5a, but with lower initial CO_2 of 2000 ppm.

The model in Figure 8 has a short cooling interval in the magma chamber prior to decompression and eruption. Therefore, the pressure drops in the inclusion associated with postentrapment cooling are limited. In consequence, the difference between the inclusion pressure and the external melt is large. Decrepitation is favored in this case compared to the higher temperature entrapment model from Figure 4a.

5.3.3. Varying Initial CO_2 Contents

If melt is trapped that is strongly undersaturated in CO_2 then substantial PEC can occur before a bubble grows. While such inclusions will not record the trapping depth because of their undersaturation, they tend to have lower inclusion overpressures and can therefore avoid decrepitation. An example of a model run with low initial CO_2 is shown in Figure 9.

5.3.4. Including Decrepitation in the Model

The process of decrepitation is likely to be controlled by number of variables that are specific to the geometry and *P-T* history of each inclusion-host system. The exchange of mass between the decrepitating inclusion and the external melt is beyond the scope of the modeling in this contribution. Nevertheless, it is possible to gain some insight into the possible role of decrepitation on the observed distribution of CO_2 contents in melt inclusions by incorporating a simplified approximation of the effects of decrepitation into the models. The results of one such model are shown in Figure 10, which uses the same host *P-T* path and initial inclusion composition as the model shown in Figure 4a. At the point when the pressure difference between the inclusion and the external melt exceeded a decrepitation threshold of 250 MPa, the pressure of the inclusion was set to that of the exterior and the CO_2 content of the inclusion melt was fixed to that for saturation at that pressure.

As expected, decrepitation causes an abrupt and significant drop in the CO_2 content of the melt inclusion. Decrepitation occurs on the decompression path in this model, and this feature of the results is likely to be generally true in cases where PEC causes a pressure drop in the inclusion. Decrepitation takes place at an external pressure of only about 30 MPa in this model, leaving an inclusion system with a CO_2 concentration

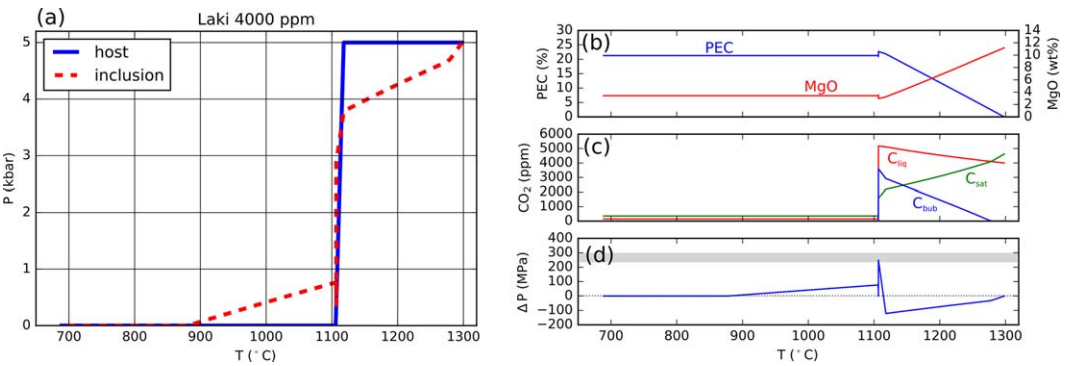

Figure 10. Identical model settings to Figure 5a, but including a decrepitation threshold at 250 MPa.

of 150 ppm. One notable feature of the model is that the pressure in the inclusion is calculated to rise after the abrupt decompression of the decrepitation event. The cause of this compression is the remelting of olivine on the inclusion walls, a consequence of the model decompression of the inclusion at fixed temperature. The model setup requires that this melting occurs after the resealing of the inclusion. In this case, the slight repressurization of the inclusion ensures that the system remains undersaturated for CO_2 as it proceeds through eruption and posteruptive cooling and therefore no vapor bubble will form. While this result is highly dependent on the details of the model setup, it is worth noting that such processes may help to account for the population of inclusions from the Laki system that contain little CO_2 in the glass and no bubble [*Hartley et al*., 2014].

6. Discussion

6.1. Can CO_2 in Inclusions Record Pressures Higher than the Decrepitation Threshold?

The model results from the previous section provide some insight into the factors that control whether melt inclusions can enter the range of overpressures where decrepitation may become possible. As expected, low entrapment pressures reduce the likelihood of decrepitation. Trapping of melt inclusions with low CO_2 contents which are far from saturation at the depth of entrapment also diminishes the opportunity for decrepitation. However, melt inclusions that are trapped with CO_2 contents below the saturation concentration cannot record their depth of entrapment.

A more important finding is that inclusions which have experienced significant cooling after their entrapment are much less likely to undergo decrepitation than those that have a short cooling interval before decompression for eruption. Postentrapment cooling allows the pressure in the inclusion to drop, forming a vapor bubble. The results of the model runs, such as those presented in Figure 7, indicate that the inclusion system can preserve information up to pressures of about twice that of the decrepitation threshold. In these cases, the bulk of the inclusion CO_2 is stored in the bubble and information about the depth of entrapment can only be recovered when the initial composition is reconstructed by measurement of both the bubble density and the glass composition.

In order to further explore the relationship between entrapment conditions and the final observed CO_2 of the inclusion system, the suite of Laki inclusion trace element compositions from *Hartley et al*. [2014] was used to estimate an initial pre-entrapment melt CO_2. Following these authors, it was assumed that the melts had a CO_2/Nb ratio of 314 prior to any degassing. The measured Nb contents of the inclusions were then used to estimate the initial CO_2 for each model run. If this initial estimate was saturated in CO_2 at the model entrapment pressure then the initial inclusion CO_2 was set to that of the saturation value. Then each inclusion was allowed to follow the same specified *P-T* path. If decrepitation does not occur then the final CO_2 content of the inclusion system of bubble plus glass matches the initial melt CO_2. The results of one such model are shown in Figure 11.

The wide range in initial CO_2 estimates reflects the large spread of observed Nb contents of the Laki inclusions, from 2.7 to 23.7 ppm. This variation in trace element contents is commonly observed in Icelandic melt inclusion suites [*Gurenko and Chaussidon*, 1995; *Maclennan*, 2008a] and is caused by variability in the mantle melt compositions supplied to individual volcanic systems [*Maclennan*, 2008b]. If these variable melts were trapped in the inclusions, then transported to the surface for eruption in a closed system, the reconstructed inclusion compositions would be equal to the trapped compositions. However, the observations show that the reconstructed inclusion compositions generally record lower CO_2, and hence P_{sat}, than expected from the estimated initial inclusion compositions (Figure 11a).

The ability of postentrapment processing to filter the original trapped distribution of melt compositions is demonstrated in Figures 11b–11d. If these melts are trapped at 4 kbar and then follow the *P-T* path depicted in Figure 7a, decrepitation is not expected to occur. In this case, reconstructed inclusion compositions can record CO_2 contents of over 4000 ppm, similar to some of the highest reconstructed inclusions based on the Laki observations. These CO_2 correspond to entrapment pressures of 4–5 kbar. In contrast, the model results shown in Figure 11c demonstrate the important role of decrepitation. Here, the initial distribution of melt compositions is trapped at 6 kbar prior to cooling, decompression, and eruption. Perhaps surprisingly, the maximum reconstructed inclusions CO_2 content predicted from this model is 3000 ppm,

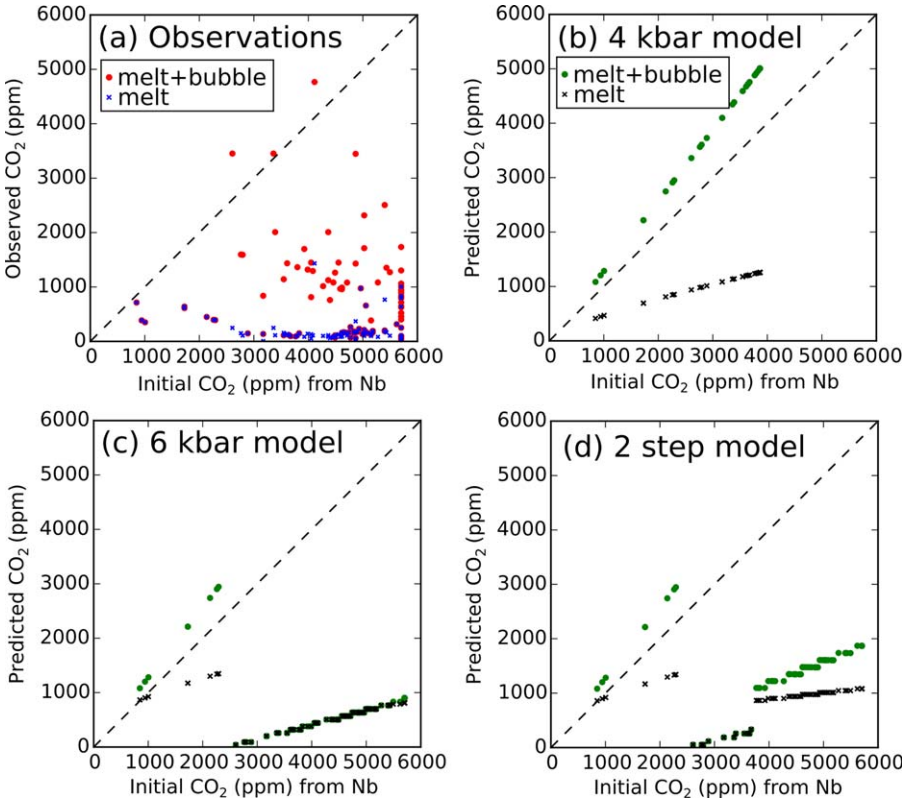

Figure 11. (a) Crosses show the observed CO_2 of the Laki melt inclusion glasses and circles show the reconstructed inclusion compositions when the observed bubble is added back to the inclusion glass. These are plotted as a function of an estimate of the initial trapped CO_2 based on the measured Nb content of the inclusions. If this estimate was higher than the predicted CO_2 saturation threshold for the model entrapment pressure, then the initial estimate was set to this saturation value. (b) Circles show model predictions for the same initial liquid composition estimates, and running them through the model *P-T* path from Figure 7, but including a decrepitation threshold at 250 MPa. Crosses show the predicted melt inclusion glass composition. (c) Same as Figure 11b, but with initial depth of entrapment at 6 kbar. (d) Same as Figure 11c, but with a two-step cooling model, with 80°C cooling at 6 kbar followed by decompression to 1.5 kbar, 100°C at that pressure, and then decompression for eruption.

less than that for the 4 kbar model. Decrepitation controls this behavior: any melt inclusions trapped with more than 3000 ppm are predicted to have decrepitated and have had their CO_2 reset at lower pressure.

The final plot, Figure 11d, shows the result of a two-step model, where entrapment takes place at 6 kbar and is followed by isobaric cooling, decompression to 1.5 kbar, further cooling, and then decompression for eruption. This path encourages deeper decrepitation of the melt inclusions with high initial CO_2, during the first decompression interval, a behavior which can be understood from Figure 5b. These inclusions are then able to preserve reconstructed melt inclusion compositions with over 1000 ppm CO_2.

The dispersion in the Laki observations, as shown in Figure 11a, cannot be generated from a single *P-T* model path. However, it is apparent that the general features of the Laki CO_2 data are consistent with the two-stage storage model suggested from the petrological thermobarometry from *Neave et al.* [2013]. In this model, primitive macrocrysts form at 4–6 kbar, cool, are transferred to a shallower melt storage zone at 1–2 kbar, and then decompressed for eruption. The cumulative distribution of expected saturation pressures for this two-step model is displayed in Figure 12 and should be compared with the observations presented in Figure 1. The model distributions show some important similarities with the observations. While entrapment of the inclusions is fixed to 6 kbar in the model, the estimated range of saturation pressures spreads from 1 to 6 kbar. This distribution reflects the spread of estimated initial CO_2 contents from the Nb-based calculation. Only about 20% of the inclusions have high enough initial CO_2 to record the entrapment pressure. Postentrapment processes leading to bubble formation and decrepitation play an important role in filtering the original distribution from entrapment. The final melt inclusion compositions are predicted to record P_{sat} that are significantly lower than the pressure distribution at the time of entrapment. None of the

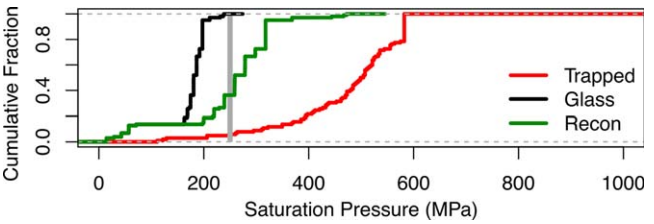

Figure 12. Cumulative distribution function plot to display results of two step decompression model from Figure 11d. The pressure of entrapment is 600 MPa and the decrepitation threshold pressure is at 250 MPa, shown as a grey vertical band. The red line shows the expected distribution of calculated saturation pressures for the originally entrapped melt inclusions, before postentrapment modification. The black line shows the distribution of P_{sat} for the predicted model melt inclusion glass compositions. The green line shows the same, but for reconstructed inclusion compositions where CO_2 stored in the bubble has been added to the glass.

inclusion glass compositions record pressures above the decrepitation threshold. An important fraction of the reconstructed inclusion compositions, where the bubble CO_2 is added back to the glass, are able to record inclusion pressures above the decrepitation threshold. A small percentage of these reconstructed inclusions record saturation pressures of up to 5 kbar, similar to the observed reconstructed compositions.

6.2. Improving Barometry

This approach of examining how postentrapment processes filter melt inclusion CO_2 contents from the initial distribution at entrapment to the final observables of glass composition and bubble density can be used to investigate whether given postentrapment *P-T* paths for the host olivines are consistent with the observations. The technique may help to resolve apparent inconsistencies in barometry, such as those outlined at the beginning of this paper. Only under certain circumstances will CO_2 in olivine-hosted melt inclusions provide useful information for barometry. If entrapment takes place at relatively low pressures, of less than 2.5 kbar in the model examples provided, then decrepitation may be avoided. For the Laki system, much less than 5% of the inclusions appear to record pressures close to the 4–6 kbar expected from independent barometry. In order to recover these pressures, it is necessary to identify samples that are likely to have had a relatively long postentrapment cooling interval. It is also apparent that large numbers of melt inclusions must be analyzed to characterize the distribution of recorded entrapment conditions for a given eruption. If small fluid inclusions are available from the same crystals as the melt inclusions, then analyses of these may provide better constraints on the depth of entrapment [*Métrich et al.*, 2014]. Similarly, targeting small melt inclusions with suitable microanalytical techniques may be used in determining entrapment pressures from CO_2 contents.

7. Conclusions

The CO_2 content of olivine-hosted melt inclusions potentially contains information about the pressure of entrapment of the inclusions and therefore the depth of crystallization in magma bodies. This signal of entrapment pressure can be obscured by a number of factors and the most important of these are likely to be undersaturation at the entrapment pressure, transfer of CO_2 to bubbles during postentrapment cooling and decrepitation of the inclusions.

Estimates of the CO_2 saturation pressure for melt inclusions from the Laki eruption appear to be inconsistent, in general, with independent estimates of crystallization depth. The distribution of CO_2-based pressures is offset to low pressures, with many inclusions returning pressures that are inconsistent with petrological and petrographic constraints on the depth and sequence of crystallization. When the CO_2 content of vapor bubbles is added back into the observed glass composition, only about 5% of the estimated saturation pressures are consistent with the independent observations, with the majority returning substantially lower pressures.

A global compilation of 2878 olivine-hosted melt inclusion compositions from mid-ocean ridges, ocean islands, Iceland, and selected continental rift zones was assembled. The calculated distribution of CO_2 saturation pressures from each of these magmatic settings is remarkably similar. The variation in melt supply rate, crustal thickness and lithospheric thickness amongst these settings is substantial and would be expected to influence the depth distribution of crystallization. If CO_2 saturation pressure recovered from melt inclusions is a faithful recorder of entrapment pressure then the distribution of these saturation pressures should vary significantly between magmatic settings. The observation that the distribution varies little from setting to setting indicates that some factor other than magma chamber depth is controlling the melt inclusion CO_2 contents.

The vast majority of inclusion saturation pressures are less than the expected decrepitation threshold of olivine hosts at ~250 MPa and the cumulative distribution of saturation pressures shows a change in gradient at pressures just beneath this threshold. These features of the observations indicate that many inclusions may have been influenced by decrepitation, such that the inclusion has ruptured during decompression of the host and has undergone loss of pressure and CO_2. The estimated saturation pressures of the reconstructed compositions of bubble-bearing inclusions are observed to exceed the decrepitation threshold.

A model was developed to track the *P-V-T-X* in melt inclusions when their olivine hosts follow a specified *P-T* path. This model was then used to understand a number of observed features of olivine-hosted melt inclusions. In this paper, the model was first used to examine the processes that control the formation of vapor bubbles. Three different factors control the saturation of CO_2 in the inclusion during postentrapment cooling of the host and crystallization of the inclusion. First, the pressure drop associated with crystallization and differential contraction lower the solubility of CO_2. Second, the crystallization raises the CO_2 content of the remaining melt. Third, the change in the major element composition of the inclusion during crystallization lower the CO_2 solubility. These three factors are of roughly equal importance.

The likelihood of decrepitation of an inclusion is influenced not only by the conditions of entrapment but also the subsequent *P-T* path followed by the host. Inclusions that are trapped at low pressure or with low CO_2 contents are less likely to decrepitate. If inclusions undergo substantial pre-eruptive cooling in magma chambers then decrepitation can sometimes be avoided, even for entrapment pressures of up to about 500 MPa. This preservation of the record of entrapment at high pressure occurs because during long cooling paths, the pressure drop inside the inclusion permits bubble formation. The inclusion system of melt and bubble can in these circumstances retain high total CO_2 at pressures beneath the decrepitation threshold.

Key features of the observed distribution of melt inclusion CO_2 in the Laki eruption can be matched by tracking the evolution of CO_2 for an ensemble of melt inclusions with varying initial CO_2 as their hosts transit a *P-T* that is consistent with independent petrological constraints on the pre-eruptive storage conditions. The apparent inconsistency between barometry based on melt inclusion CO_2 and constraints from other barometers can be resolved by consideration of three factors. First, that trace element evidence for heterogeneity in the trapped melt composition is reflected in varying initial CO_2. Second, that inclusion *P-T-V-X* is tracked along a specified *P-T* derived from independent barometry. Third, that decrepitation is included in the models.

Acknowledgments

I would like to thank the Royal Society (IE150300) and the Natural Environment Research Council (NE/I012508/1) for funding. Data for the global compilation of melt inclusion composition was taken from published literature as cited in the text, but also available as a table in a supporting information file. Woods Hole Oceanographic Institution kindly provided sabbatical space and an adjunct position. Glenn Gaetani and Adam Soule are particularly thanked for their assistance at Woods Hole. Comments and criticism from Oli Shorttle, Margaret Hartley, and David Neave helped to improve the first draft of this manuscript. Formal reviews by Matthew Steele-MacInnis and an anonymous reviewer are greatly appreciated, and hopefully helped to make this contribution more accessible to the fluid inclusion community. The editorial patience of Cin-Ty Lee is also gratefully acknowledged.

References

Anderson, A. T., and G. G. Brown (1993), CO2 contents and formation pressures of some Kilauean melt inclusions, *Am. Mineral.*, *78*(7–8), 794–803.

Annen, C., and R. S. J. Sparks (2002), Effects of repetitive emplacement of basaltic intrusions on thermal evolution and melt generation in the crust, *Earth Planet. Sci. Lett.*, *203*(3), 937–955.

Aster, E. M., P. J. Wallace, L. R. Moore, J. Watkins, E. Gazel, and R. J. Bodnar (2016), Reconstructing CO_2 concentrations in basaltic melt inclusions using Raman analysis of vapor bubbles, *J. Volcanol. Geotherm. Res.*, *323*, 148–162.

Beattie, P. (1993), Olivine-melt and orthopyroxene-melt equilibria, *Contrib. Mineral. Petrol.*, *115*(1), 103–111.

Bodnar, R. J., and P. M. Bethke (1984), Systematic stretching of fluid inclusions I: Fluorite and sphalerite at 1 atmosphere confining pressure, *Econ. Geol.*, *79*(1), 141–161.

Bucholz, C. E., G. A. Gaetani, M. D. Behn, and N. Shimizu (2013), Post-entrapment modification of volatiles and oxygen fugacity in olivine-hosted melt inclusions, *Earth Planet. Sci. Lett.*, *374*, 145–155.

Cabral, R. A., M. G. Jackson, K. T. Koga, E. F. Rose-Koga, E. H. Hauri, M. J. Whitehouse, A. A. Price, J. Day, N. Shimizu, and K. A. Kelley (2014), Volatile cycling of H_2O, CO_2, F, and Cl in the HIMU mantle: A new window provided by melt inclusions from oceanic hot spot lavas at Mangaia, Cook Islands, *Geochem. Geophys. Geosyst.*, *15*, 4445–4467, doi:10.1002/2014GC005473.

Campione, M., N. Malaspina, and M. L. Frezzotti (2015), Threshold size for fluid inclusion decrepitation, *J. Geophys. Res. Solid Earth*, *120*, 7396–7402, doi:10.1002/2015JB012086.

Cervantes, P., and P. Wallace (2003), Role of H_2O in subduction-zone magmatism: New insights from melt inclusions in high-Mg basalts from central Mexico, *Geology*, *31*(3), 235–238, doi:10.1130/0091-7613(2003)0312.0.CO;2.

Chen, Y., A. Provost, P. Schiano, and N. Cluzel (2011), The rate of water loss from olivine-hosted melt inclusions, *Contrib. Mineral. Petrol.*, *162*(3), 625–636, doi:10.1007/s00410-011-0616-5.

Colman, A., J. M. Sinton, and V. D. Wanless (2015), Constraints from melt inclusions on depths of magma residence at intermediate magma supply along the Galápagos spreading center, *Earth Planet. Sci. Lett.*, *412*, 122–131.

Danyushevsky, L. V. (2002), Melt inclusions in olivine phenocrysts: Using diffusive re-equilibration to determine the cooling history of a crystal, with implications for the origin of olivine-phyric volcanic rocks, *J. Petrol.*, *43*(9), 1651–1671, doi:10.1093/petrology/43.9.1651.

Danyushevsky, L. V., and P. Plechov (2011), Petrolog3: Integrated software for modeling crystallization processes, *Geochem. Geophys. Geosyst.*, *12*, Q07021, doi:10.1029/2011GC003516.

Di Muro, A., N. Métrich, D. Vergani, M. Rosi, P. Armienti, T. Fougeroux, E. Deloule, I. Arienzo, and L. Civetta (2014), The shallow plumbing system of Piton de la Fournaise volcano (La Reunion island, Indian Ocean) revealed by the major 2007 caldera-forming eruption, *J. Petrol.*, *55*(7), 1287–1315.

Dingwell, D. B., and S. L. Webb (1990), Relaxation in silicate melts, *Eur. J. Mineral.*, *2*(4), 427–449.

Dixon, J., E. Stolper, and J. Holloway (1995), An experimental study of water and carbon dioxide solubilities in mid ocean ridge basaltic liquids.1. Calibration and solubility models, *J. Petrol.*, *36*(6), 1607–1631.
Dodson, M. H. (1973), Closure temperature in cooling geochronological and petrological systems, *Contrib. Mineral. Petrol.*, *40*(3), 259–274.
Esposito, R., R. J. Bodnar, L. V. Danyushevsky, B. De Vivo, L. Fedele, J. Hunter, A. Lima, and N. Shimizu (2011), Volatile evolution of magma associated with the Solchiaro Eruption in the Phlegrean Volcanic District (Italy), *J. Petrol.*, *52*(12), 2431–2460, doi:10.1093/petrology/egr051.
Gaetani, G. A., and E. Watson (2000), Open system behavior of olivine-hosted melt inclusions, *Earth Planet. Sci. Lett.*, *183*(1–2), 27–41, doi:10.1016/S0012-821X(00)00260-0.
Gaetani, G. A., J. A. O'Leary, N. Shimizu, C. E. Bucholz, and M. Newville (2012), Rapid reequilibration of H_2O and oxygen fugacity in olivine-hosted melt inclusions, *Geology*, *40*(10), 915–918, doi:10.1130/G32992.1.
Garcia, M. O. (2000), Magmatic processes during the prolonged Pu'u 'O'o eruption of Kilauea Volcano, Hawaii, *J. Petrol.*, *41*(7), 967–990, doi:10.1093/petrology/41.7.967.
Geist, D. J., G. Bergantz, and W. W. Chadwick (2014), Galápagos Magma Chambers, in *The Galapagos: A Natural Laboratory for the Earth Sciences*, edited by K. S. Harpp, E. Mittelstaedt, N. d'Ozouville and D. W. Graham, vol. 204, 55 pp., John Wiley & Sons, Inc, Hoboken, N. J., doi:10.1002/9781118852538.ch5.
Giordano, D., J. K. Russell, and D. B. Dingwell (2008), Viscosity of magmatic liquids: A model, *Earth Planet. Sci. Lett.*, *271*(1), 123–134.
Gottsmann, J., A. J. Harris, and D. B. Dingwell (2004), Thermal history of Hawaiian pāhoehoe lava crusts at the glass transition: Implications for flow rheology and emplacement, *Earth Planet. Sci. Lett.*, *228*(3), 343–353.
Guilbaud, M., S. Blake, T. Thordarson, and S. Self (2007), Role of syn-eruptive cooling and degassing on textures of lavas from the AD 1783–1784 Laki eruption, south Iceland, *J. Petrol.*, *48*, 1265–1294.
Guiraud, M., and R. Powell (2006), P-V-T relationships and mineral equilibria in inclusions in minerals, *Earth Planet. Sci. Lett.*, *244*(3), 683–694.
Gurenko, A. A., and M. Chaussidon (1995), Enriched and depleted primitive melts included in olivine from Icelandic tholeiites: Origin by continuous melting of a single mantle column, *Geochim. Cosmochim. Acta*, *59*(14), 2905–2917.
Hartley, M. E., J. Maclennan, M. Edmonds, and T. Thordarson (2014), Reconstructing the deep CO_2 degassing behaviour of large basaltic fissure eruptions, *Earth Planet. Sci. Lett.*, *393*, 120–131, doi:10.1016/j.epsl.2014.02.031.
Hartley, M. E., D. A. Neave, J. Maclennan, T. Thordarson, and M. Edmonds (2015), Diffusive over-hydration of olivine-hosted melt inclusions, *Earth Planet. Sci. Lett.*, *425*, 168–178, doi:10.1016/j.epsl.2015.06.008.
Head, E. M., A. M. Shaw, P. J. Wallace, K. W. Sims, and S. A. Carn (2011), Insight into volatile behavior at Nyamuragira volcano (D.R. Congo, Africa) through olivine-hosted melt inclusions, *Geochem. Geophys. Geosyst.*, *12*, Q0AB11, doi:10.1029/2011GC003699.
Holland, T., and R. Powell (1991), A compensated-Redlich-Kwong (CORK) equation for volumes and fugacities of CO_2 and H_2O in the range 1 bar to 50 kbar and 100–1600°C, *Contrib. Mineral. Petrol.*, *109*(2), 265–273.
Holland, T., and R. Powell (2011), An improved and extended internally consistent thermodynamic dataset for phases of petrological interest, involving a new equation of state for solids, *J. Metamorph. Geol.*, *29*(3), 333–383.
Hudgins, T. R., S. B. Mukasa, A. C. Simon, G. Moore, and E. Barifaijo (2015), Melt inclusion evidence for CO_2-rich melts beneath the western branch of the East African Rift: Implications for long-term storage of volatiles in the deep lithospheric mantle, *Contrib. Mineral. Petrol.*, *169*(5), 46, doi:10.1007/s00410-015-1140-9.
Kamenetsky, V. S., M. Pompilio, N. Métrich, A. V. Sobolev, D. V. Kuzmin, and R. Thomas (2007), Arrival of extremely volatile-rich high-Mg magmas changes explosivity of Mount Etna, *Geology*, *35*(3), 255–258.
Koleszar, A., A. Saal, E. Hauri, A. Nagle, Y. Liang, and M. Kurz (2009), The volatile contents of the Galapagos plume: Evidence for H_2O and F open system behavior in melt inclusions, *Earth Planet. Sci. Lett.*, *287*(3), 442–452.
Kress, V. C., and I. S. Carmichael (1991), The compressibility of silicate liquids containing Fe_2O_3 and the effect of composition, temperature, oxygen fugacity and pressure on their redox states, *Contrib. Mineral. Petrol.*, *108*(1–2), 82–92.
Lange, R., and I. S. Carmichael (1990), Thermodynamic properties of silicate liquids with emphasis on density, thermal expansion and compressibility, *Rev. Mineral. Geochem.*, *24*(1), 25–64.
Lange, R. A., and A. Navrotsky (1992), Heat capacities of Fe_2O_3-bearing silicate liquids, *Contrib. Mineral. Petrol.*, *110*(2–3), 311–320.
Lloyd, A. S., T. Plank, P. Ruprecht, E. H. Hauri, and W. Rose (2013), Volatile loss from melt inclusions in pyroclasts of differing sizes, *Contrib. Mineral. Petrol.*, *165*(1), 129–153.
Lowenstern, J. B. (1995), Applications of silicate-melt inclusions to the study of magmatic volatiles, *Magmas Fluids Ore Deposits*, *23*, 71–99.
Maclennan, J. (2008a), Concurrent mixing and cooling of melts under Iceland, *J. Petrol.*, *49*(11), 1931–1953.
Maclennan, J. (2008b), Lead isotope variability in olivine-hosted melt inclusions from Iceland, *Geochim. Cosmochim. Acta*, *72*(16), 4159–4176.
Maclennan, J., D. McKenzie, K. Grönvold, N. Shimizu, J. Eiler, and N. Kitchen (2003), Melt mixing and crystallization under Theistareykir, northeast Iceland, *Geochem. Geophys. Geosyst.*, *4*(11), 8624, doi:10.1029/2003GC000558.
Massare, D., N. Métrich, and R. Clocchiatti (2002), High-temperature experiments on silicate melt inclusions in olivine at 1 atm: Inference on temperatures of homogenization and H_2O concentrations, *Chem. Geol.*, *183*(1–4), 87–98, doi:10.1016/S0009-2541(01)00373-4.
McKenzie, D., and M. Bickle (1988), The volume and composition of melt generated by extension of the lithosphere, *J. Petrol.*, *29*(3), 625–679.
Metrich, N., and P. J. Wallace (2008), Volatile abundances in basaltic magmas and their degassing paths tracked by melt inclusions, *Rev. Mineral. Geochem.*, *69*(1), 363–402, doi:10.2138/rmg.2008.69.10.
Métrich, N., V. Zanon, L. Créon, A. Hildenbrand, M. Moreira, and F. O. Marques (2014), Is the 'Azores hotspot' a wetspot? Insights from the geochemistry of fluid and melt inclusions in olivine of Pico basalts, *J. Petrol.*, *55*(2), 377–393.
Mironov, N., M. Portnyagin, R. Botcharnikov, A. Gurenko, K. Hoernle, and F. Holtz (2015), Quantification of the CO_2 budget and H_2O-CO_2 systematics in subduction-zone magmas through the experimental hydration of melt inclusions in olivine at high H_2O pressure, *Earth Planet. Sci. Lett.*, *425*, 1–11, doi:10.1016/j.epsl.2015.05.043.
Moore, L. R., E. Gazel, R. Tuohy, A. S. Lloyd, R. Esposito, M. Steele-MacInnis, E. H. Hauri, P. J. Wallace, T. Plank, and R. J. Bodnar (2015), Bubbles matter: An assessment of the contribution of vapor bubbles to melt inclusion volatile budgets, *Am. Mineral.*, *100*(4), 806–823, doi:10.2138/am-2015-5036.
Morgan, J. P., and Y. J. Chen (1993), The genesis of oceanic crust: Magma injection, hydrothermal circulation, and crustal flow, *J. Geophys. Res. Solid Earth*, *98*(B4), 6283–6297.
Mysen, B. O., R. J. Arculus, and D. H. Eggler (1975), Solubility of carbon dioxide in melts of andesite, tholeiite, and olivine nephelinite composition to 30 kbar pressure, *Contrib. Mineral. Petrol.*, *53*(4), 227–239, doi:10.1007/BF00382441.

Neave, D., E. Passmore, J. Maclennan, G. Fitton, and T. Thordarson (2013), Crystal-melt relationships and the record of deep mixing and crystallization in the AD 1783 Laki eruption, Iceland, *J. Petrol.*, *54*, 1661–1690.
Neave, D. A., J. Maclennan, M. Edmonds, and T. Thordarson (2014), Melt mixing causes negative correlation of trace element enrichment and CO_2 content prior to an Icelandic eruption, *Earth Planet. Sci. Lett.*, *400*, 272–283, doi:10.1016/j.epsl.2014.05.050.
Neave, D. A., J. Maclennan, T. Thordarson, and M. E. Hartley (2015), The evolution and storage of primitive melts in the Eastern Volcanic Zone of Iceland: The 10 ka Grímsvötn tephra series (i.e., the Saksunarvatn ash), *Contrib. Mineral. Petrol.*, *170*(2), 1–23, doi:10.1007/s00410-015-1170-3.
Ni, H., and H. Keppler (2013), Carbon in silicate melts, *Rev. Mineral. Geochem.*, *75*(1), 251–87.
Nichols, A., M. Potuzak, and D. Dingwell (2009), Cooling rates of basaltic hyaloclastites and pillow lava glasses from the HSDP2 drill core, *Geochim. Cosmochim. Acta*, *73*(4), 1052–1066.
Núñez-Valdez, M., K. Umemoto, and R. Wentzcovitch (2010), Fundamentals of elasticity of $(Mg_{1-x}, Fex)_2SiO_4$ olivine, *Geophys. Res. Lett.*, *37*(14).
Ochs, F. A., and R. A. Lange (1999), The density of hydrous magmatic liquids, *Science*, *283*(5406), 1314–1317.
Oppenheimer, C., R. Moretti, P. R. Kyle, A. Eschenbacher, J. B. Lowenstern, R. L. Hervig, and N. W. Dunbar (2011), Mantle to surface degassing of alkalic magmas at Erebus volcano, Antarctica, *Earth Planet. Sci. Lett.*, *306*(3), 261–271.
Passmore, E., J. Maclennan, G. Fitton, and T. Thordarson (2012), Mush disaggregation in basaltic magma chambers: Evidence from the AD 1783 Laki eruption, *J. Petrol.*, *53*, 2593–2623.
Portnyagin, M. V., N. L. Mironov, S. V. Matveev, and P. Yu. Plechov (2005), Petrology of Avachites, high-Magnesian basalts of Avachinsky Volcano, Kamchatka: II. Melt inclusions in olivine, *Petrology*, *13*(4), 322–351.
Putirka, K. D. (2008), Thermometers and barometers for volcanic systems, *Rev. Mineral. Geochem.*, *69*(1), 61–120.
Roedder, E. (1965), Liquid CO_2 inclusions in olivine-bearing nodules and phenocrysts from basalts, *Am. Mineral.*, *50*, 1746–1782.
Roedder, E. (1984), Fluid inclusions, *Rev. Mineral.*, *12*.
Saal, A. E., E. H. Hauri, C. H. Langmuir, and M. R. Perfit (2002), Vapour undersaturation in primitive mid-ocean-ridge basalt and the volatile content of Earth's upper mantle, *Nature*, *419*(6906), 451–455, doi:10.1038/nature01073.
Schiavi, F., A. Provost, P. Schiano, and N. Cluzel (2016), P-V-T-X evolution of olivine-hosted melt inclusions during high-temperature homogenization treatment, *Geochim. Cosmochim. Acta*, *172*, 1–21, doi:10.1016/j.gca.2015.09.025.
Shaw, A. M., M. D. Behn, S. E. Humphris, R. A. Sohn, and P. M. Gregg (2010), Deep pooling of low degree melts and volatile fluxes at the 85°E segment of the Gakkel Ridge: Evidence from olivine-hosted melt inclusions and glasses, *Earth Planet. Sci. Lett.*, *289*(3–4), 311–322, doi:10.1016/j.epsl.2009.11.018.
Shishkina, T. A., R. E. Botcharnikov, F. Holtz, R. R. Almeev, A. M. Jazwa, and A. A. Jakubiak (2014), Compositional and pressure effects on the solubility of H_2O and CO_2 in mafic melts, *Chem. Geol.*, *388*, 112–129, doi:10.1016/j.chemgeo.2014.09.001.
Sides, I., M. Edmonds, J. Maclennan, B. Houghton, D. Swanson, and M. Steele-MacInnis (2014), Magma mixing and high fountaining during the 1959 Kilauea Iki eruption, Hawai'i, *Earth Planet. Sci. Lett.*, *400*, 102–112, doi:10.1016/j.epsl.2014.05.024.
Sobolev, A. V., and L. V. Danyushevsky (1994), Petrology and geochemistry of boninites from the north termination of the Tonga Trench: Constraints on the generation conditions of primary high-Ca boninite magmas, *J. Petrol.*, *35*(5), 1183–1211, doi:10.1093/petrology/35.5.1183.
Steele-Macinnis, M., R. Esposito, and R. J. Bodnar (2011), Thermodynamic Model for the effect of post-entrapment crystallization on the H_2O-CO_2 systematics of vapor-saturated, silicate melt inclusions, *J. Petrol.*, *52*(12), 2461–2482, doi:10.1093/petrology/egr052.
Stolper, E., and J. R. Holloway (1988), Experimental determination of the solubility of carbon dioxide in molten basalt at low pressure, *Earth Planet. Sci. Lett.*, *87*(4), 397–408, doi:10.1016/0012-821X(88)90004-0.
Sugawara, T. (2000), Empirical relationships between temperature, pressure, and MgO content in olivine and pyroxene saturated liquid, *J. Geophys. Res. Solid Earth*, *105*(B4), 8457–8472.
Tait, S. (1992), Selective preservation of melt inclusions in igneous phenocrysts, *Am. Mineral.*, *77*(1–2), 146–155.
Thomson, A., and J. Maclennan (2013), The distribution of olivine compositions in Icelandic basalts and picrites, *J. Petrol.*, *54*(4), 745–768, doi:10.1093/petrology/egs083.
Thordarson, T., and S. Self (1993), The Laki (Skaftár Fires) and Grímsvötn eruptions in 1783–1785, *Bull. Volcanol.*, *55*, 233–263.
Wallace, P. J., V. S. Kamenetsky, and P. Cervantes (2015), Melt inclusion CO_2 contents, pressures of olivine crystallization, and the problem of shrinkage bubbles, *Am. Mineral.*, *100*(4), 787–794, doi:10.2138/am-2015-5029.
Wanamaker, B., T.-F. Wong, and B. Evans (1990), Decrepitation and crack healing of fluid inclusions in San Carlos olivine, *J. Geophys. Res.*, *95*(B10), 15,623–15,641.
Wanless, V., M. Behn, A. Shaw, and T. Plank (2014), Variations in melting dynamics and mantle compositions along the eastern volcanic zone of the Gakkel Ridge: Insights from olivine-hosted melt inclusions, *Contrib. Mineral. Petrol.*, *167*(5), 1–22.
Wanless, V. D., and A. M. Shaw (2012), Lower crustal crystallization and melt evolution at mid-ocean ridges, *Nat. Geosci.*, *5*(9), 651–655, doi:10.1038/ngeo1552.
Wanless, V. D., A. M. Shaw, M. D. Behn, S. A. Soule, J. Escartin, and C. Hamelin (2015), Magmatic plumbing at lucky strike volcano based on olivine-hosted melt inclusion compositions, *Geochem. Geophys. Geosyst.*, *16*, 126–147.
Winpenny, B., and J. Maclennan (2011), A partial record of mixing of mantle melts preserved in Icelandic phenocrysts, *J. Petrol.*, *52*(9), 1791–1812.
Winpenny, B., and J. Maclennan (2014), Short length scale oxygen isotope heterogeneity in the Icelandic mantle: Evidence from plagioclase compositional zones, *J. Petrol.*, *55*(12), 2537–2566.
Yang, H.-J., R. J. Kinzler, and T. Grove (1996), Experiments and models of anhydrous, basaltic olivine-plagioclase-augite saturated melts from 0.001 to 10 kbar, *Contrib. Mineral. Petrol.*, *124*(1), 1–18.
Zhang, Y. (1998), Mechanical and phase equilibria in inclusion-host systems, *Earth Planet. Sci. Lett.*, *157*(3), 209–222.